applied sciences

MDPI

Article

Optimized Geographical Distribution of Robotic Observatory Networks for Space Surveillance and Tracking Using Goldberg Polyhedra and Voronoi Tessellations

Francisco Espartero [1,2], Adrián Rodríguez-Jiménez [3], Javier Cubas [1] and Santiago Pindado [1,*]

[1] Escuela Técnica Superior de Ingeniería Aeronáutica y del Espacio (ETSIAE), Universidad Politécnica de Madrid (UPM), 28040 Madrid, Spain; fa.espartero@alumnos.upm.es (F.E.); j.cubas@upm.es (J.C.)
[2] ECS Engineering & Astrophysics, Santa Mónica 8 bajo, Alcalá de Henares, 28804 Madrid, Spain
[3] Ingeniería de Sistemas para la Defensa de España (ISDEFE), S.A., Beatriz de Bobadilla 3, Moncloa-Aravaca, 28040 Madrid, Spain
* Correspondence: santiago.pindado@upm.es

Abstract

The deployment of global robotic observatory networks requires a station distribution that ensures geometrical visibility coverage of space objects while minimizing the number of ground-based stations. This work proposes a geometrical framework combining visibility constraints, Goldberg polyhedra, and Voronoi tessellations to determine this distribution. The methodology relates orbital altitude and minimum observation elevation above the horizon to the angular separation required between observatories, estimating the number of stations from a spacing criterion. A GIS-based optimization procedure is then applied to maximize the placement of observatories over continental land masses through systematic rotation of the resulting configurations. The method is evaluated for orbital altitudes from 100 km to 2000 km and minimum observation elevations of 20° and 30°. Results show that the number of observatories estimated with a spacing criterion ranges from 6252 stations at 100 km to only 42 stations at 2000 km, with similar proportions of stations on land for the Goldberg and Voronoi configurations (between 29% and 50%, with differences below 2.4 percentage points). Case studies for Australia, Ukraine, and Ecuador show that reorienting the configuration to a specific territory increases the number of stations located inside it, with larger relative gains in the smaller territories. The proposed framework provides a practical tool for the design and planning of robotic observatory networks for Space Surveillance and Tracking applications.

Keywords: robotic observatory networks; Goldberg polyhedra; Voronoi tessellation; geometrical optimization; Space Surveillance and Tracking (SST); Resident Space Objects (RSOs)

Check for updates

Academic Editor: Wei Huang

Received: 28 September 2026
Revised: 20 October 2026
Accepted: 20 October 2026
Published: 22 October 2026

Copyright: © 2026 by the authors. Licensee MDPI, Basel, Switzerland. This article is an open access article distributed under the terms and conditions of the Creative Commons Attribution (CC BY) license.

1. Introduction

The observation and monitoring of objects in near-Earth space has become increasingly important for both scientific research and the safe operation of space activities. During the 20th century, several campaigns were carried out to detect and monitor near-Earth objects (NEOs) using various types of sensors, including video and still cameras. In combination with wide-field optical systems and telescopes, these instruments enabled significant advances in the study of natural objects located in the vicinity of the Earth [1]. These efforts led to major advances in research on meteor showers, fireballs and meteorites [2], as well as

to the discovery of comets and the identification of potentially hazardous asteroids because of the risk of collision with our planet [3].

The detailed study of natural objects posing a collision risk has also driven substantial advances in observational instrumentation and in the development of specialized software for data processing and analysis [4]. These improvements have enabled a more precise characterization and determination of the orbits of the detected objects [5], which has made it possible not only to identify their nature but also, in some cases, to determine their parent body [6].

In recent decades, with the rapid growth in the number of artificial satellites, optical and near-infrared systems traditionally employed in astrophysics have increasingly been adapted for the surveillance and detection of artificial space objects [7]. Artificial Resident Space Objects (RSOs) can be detected using techniques similar to those applied to the study of minor bodies of the Solar System [8] and potentially hazardous NEOs [9]. Furthermore, both the hardware (sensors, cameras, and telescopes) and the software developed for image processing have demonstrated significant capabilities when applied to the detection and surveillance of artificial satellites [10,11].

This growth, driven by the deployment of large constellations in Low Earth Orbit (LEO) and Very Low Earth Orbit (VLEO) and by the rising launch activity of both countries and private companies, has been accompanied by a growing number of space objects on re-entry trajectories [12,13]. These developments have introduced a range of associated risks, including uncontrolled rocket-body re-entries, defunct satellites, operational failures, collisions, and the continuous growth of space debris, all of which represent an increasing challenge for space monitoring systems [14].

At present, assessing these threats, particularly those associated with objects in VLEO and re-entry trajectories, relies on the continuous surveillance of near-Earth space, the determination of object trajectories, and the prediction of potential impacts [15]. Consequently, the development of accurate and reliable Space Surveillance and Tracking (SST) systems capable of monitoring objects at very low altitudes has become an essential requirement [16].

As in the case of NEO monitoring, detection systems typically integrate telescopes, cameras, and sensors within a single observatory infrastructure [17]. The effectiveness of these systems has improved substantially through the combination and cross-validation of observations acquired from multiple observatories operating in real time [18]. Combining data from different locations allows more accurate trajectory estimation and orbital determination of the observed object [15].

This multi-observatory approach was first employed for the observation and tracking of meteors and meteoroids during the final decades of the twentieth century [4,19]. Since a meteor remains visible only during the brief interval of atmospheric ablation [5], multiple observing stations are required to determine its trajectory and orbital parameters accurately. Meteor observation networks are typically composed of stations separated by distances ranging from 100 to 400 km [5]. However, when monitoring space objects over larger geographical regions, observatories distributed across different locations become necessary. An appropriate distribution can improve the accuracy of trajectory estimation through observations from multiple sites, provide redundancy and geometrical continuity in the monitoring process, and reduce the number of observatories required to achieve a given level of coverage. Consequently, both the number and the geographical distribution of observatories become relevant factors in the design of an effective and efficient surveillance network.

At present, only a limited number of dedicated networks have been established for the surveillance and tracking of RSOs [20–23] and other space objects. Among existing robotic astronomical networks, the BOOTES network should be mentioned. Although

its primary mission is the study of gamma-ray bursts (GRBs), supernovae, and other high-energy astrophysical phenomena, it is a network of robotic observatories that started in Spain in 1998 [24] and was extended to the southern hemisphere in 2009 with a station in New Zealand [25]. However, the decreasing cost of observational technologies and the development of low-cost Robotic Space Object Observatories (ROSOs) [26] provide an opportunity to design synchronized networks with large geographical coverage for monitoring satellite objects across different orbital regimes. ROSOs constitute an attractive solution for constructing such networks because they are modular, versatile, and easily transportable, enabling rapid deployment at relatively low cost.

Existing network-planning studies address the problem from different angles. ISON [20] and APOSOS [21] rely on collaborating institutions and site surveys; Zhulong [23] assesses the accuracy of an operating network; BOOTES [24,25] was deployed from existing institutional facilities; and Urru et al. [22] optimize the choice of sites within a finite list of candidates using catalog propagation and a detection-based performance index. In all these cases, the layout is conditioned by a predefined set of candidate sites or by a reference catalog. To the best of our knowledge, no general relation has been proposed that links the altitude of the target orbital regime and the minimum elevation of the telescopes directly to the spacing and number of stations needed for homogeneous global coverage. This work addresses that gap by deriving the station spacing and number from altitude and elevation (Sections 3 and 4) and then evaluating how the resulting networks can be oriented to maximize land-based sites (Section 5). Since the ideal hexagonal arrangement cannot be mapped onto a sphere, spherical tilings are required: Goldberg polyhedra are used as the main framework, as they preserve nearly regular hexagonal cells (plus 12 pentagons), and Voronoi tessellations, which admit an arbitrary number of sites, are used as a comparative reference.

In this context, the present work aims to provide a geometrical framework for determining the number and geographical distribution of observatories required to support the efficient planning of global ROSO networks for the surveillance and tracking of RSOs at different orbital altitudes. The study focuses on altitudes ranging from VLEO to approximately 2000 km, encompassing the orbital regions that currently host the highest concentration of satellites and space traffic. For this purpose, the effective coverage provided by each observatory is related to the altitude of the RSO and to the minimum elevation angle above the horizon required for reliable observation. The separation between neighboring observatories is then determined to provide sufficient overlap between their observable regions, while the spherical geometry of the Earth and the distribution of continental land masses are taken into account when determining suitable station locations.

These requirements naturally lead to a geometrical optimization problem, in which the Earth's surface must be divided into suitable observation regions while maintaining the required overlap between neighboring stations. Geometrical tessellations and spherical discretization techniques have been successfully applied to a variety of astronomical and astrophysical problems. Voronoi tessellations have been used for the analysis of large-scale galaxy distributions, cluster identification, image processing, adaptive spatial binning, spectroscopic data analysis, and cosmological simulations, demonstrating their usefulness as tools for spatial partitioning and optimization in astronomy [27]. Likewise, spherical geometry and tessellation-based representations have been employed to describe astronomical survey footprints, sky coverage, and large observational datasets on the celestial sphere [28]. More recently, Goldberg polyhedra have been adopted for planetary-scale spatial discretization and numerical modeling, providing an efficient framework for representing and analyzing global processes on spherical surfaces [29]. However, to the best of our knowledge, neither Goldberg polyhedra nor Voronoi tessellations have previously been

employed for the planning and optimization of global networks of robotic observatories dedicated to Space Surveillance and Tracking applications.

Based on these geometrical approaches, the required number and geographical distribution of observatories are analyzed using Goldberg polyhedra [30,31] and Voronoi tessellations [32], adapted to the spherical geometry of the Earth and considering both atmospheric limitations and sky-visibility constraints.

The remainder of this paper is organized as follows. Section 2 introduces the main factors affecting the observation and orbital determination of RSOs, including atmospheric visibility constraints. Section 3 develops the visibility model and derives the geometrical relationships required to estimate the area covered by individual observatories and the overlap between neighboring stations. Section 4 presents the Goldberg- and Voronoi-based distribution frameworks used to support the planning of global observatory networks and estimate the number and separation of observatories required for different orbital altitudes and visibility constraints. Section 5 describes the GIS-based optimization procedure adopted to maximize the placement of observatories on terrestrial landmasses. Section 6 presents the results obtained from the global optimization and the regional case studies for Australia, Ukraine, and Ecuador. Finally, Section 7 summarizes the main conclusions and implications of the proposed geometrical framework.

2. Optical Observation Constraints for Resident Space Objects

Optical observation of RSOs is subject to several constraints that affect both their detectability and the quality of the measurements obtained from ground-based observatories. RSOs are visible in the optical and near-infrared spectral range provided that, from the observer's perspective, the object is above the horizon and illuminated by the Sun, so that it can reflect light. Furthermore, it is very important that the atmosphere is free from significant aerosols and light pollution, and that the sky is clear and cloudless.

In the case of artificial satellites and space debris, it should also be borne in mind that they are only visible when they reflect sunlight. It will therefore be very difficult to determine their actual position when they pass through the Earth's shadow [33] and, depending on the altitude of their orbit, they will be visible for only a very short stretch of their trajectory (and for a brief period of time).

To detect satellites, it is essential that optical telescopes are correctly positioned and that the sky brightness at the zenith is at least 18 mag/arcsec^2 during nautical twilight (when the Sun is 12° below the horizon), and slightly higher during astronomical twilight (or when the Sun is 18° below the horizon). The lower the Sun, the darker the sky, so that fainter objects become detectable as darkness falls. The higher the value of mag/arcsec^2, the better the visibility of the satellite. At twilight (the same applies to dawn, but in reverse), the typical brightness of the sky at the zenith (without the Sun, but with daylight) is around 8 mag/arcsec^2, increasing progressively as darkness falls, up to around 18 mag/arcsec^2 (about two hours after twilight) at progressive angles of solar declination [34].

Besides the time of day, the lighting conditions of RSOs depend on the observer's latitude and the season (for example, a site located at 45° north retains some visibility of illuminated LEO objects throughout the night in summer). Furthermore, the operation of these systems at lower elevation angles dramatically increases the number of visible orbits of satellites in LEO. Indeed, approximately 90% of space debris observations are made at elevation angles below 50° [35].

Low-altitude RSOs in LEO can exceed angular velocities of one degree per second relative to a ground-based observer when observed from high elevation angles. The apparent angular velocity therefore represents an additional constraint for optical tracking, particularly for objects in LEO and VLEO. In such cases, it is preferable to observe them

with a large-aperture telescope [33]. For a circular orbit, and neglecting the rotation of the Earth, the apparent angular velocity of an RSO passing through the zenith of the observer is approximately 1.48, 0.72 and 0.27°/s at altitudes of 300, 600 and 1500 km, respectively. At an elevation angle of 30°, the maximum values, for a pass in the vertical plane containing the observer, are approximately 0.44, 0.25 and 0.12°/s for the same altitudes. For a given elevation, the angular velocity therefore decreases as the orbital altitude increases, and for a given altitude it reaches its maximum when the object passes through the zenith.

RSOs are not visible when they are between the Earth and the Sun, or when they pass through the Earth's shadow. They are only visible after sunset (at the observation point) and until the RSO enters the Earth's shadow, and between the moment it leaves the Earth's shadow and sunrise (at the observation point) [16]. Furthermore, the 23° 27′ inclination of the Earth's axis of rotation has the effect of lengthening the observation period in summer and shortening it in winter. Finally, it should be noted that the Earth's shadow cone includes penumbral zones in the orbits of RSOs that allow for partial observation [10]. These conditions are not included in the geometrical model of Sections 3 and 4, which considers only the visibility of an object above a minimum elevation (see the limitations discussed in the Conclusions of the present paper).

The view of the sky from any point on the Earth's surface is limited by the horizon. Leaving weather conditions aside, the observation of an RSO depends on a minimum elevation and sufficient brightness for it to be detected [36]. Furthermore, a minimum angle above the horizon is required for a proper observation; this angle is set at around 20° (see Figure 1) [37], although, in poor atmospheric conditions, measurements at angles below 30° may need to be discarded. This is due to atmospheric refraction, which significantly distorts measurements of an RSO with respect to its actual position. The parameters influencing good RSO observations include the altitude of their orbits, the elevation of the observatory's field of view above the horizon, and the distribution of telescopes, including their ability to overlap their fields of view so that an object can be followed geometrically without observations at unfavorable angles. On the other hand, the loss of precision in observations made by telescopes in areas close to the horizon, due to refraction and other factors, could be compensated for if multiple observations were available for those areas.

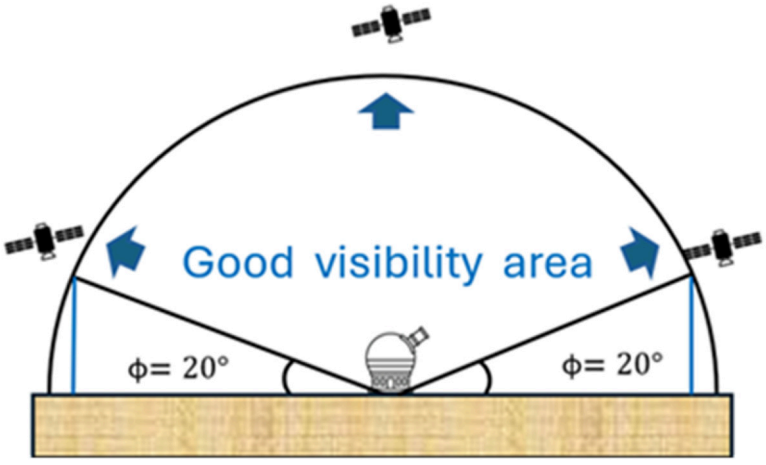


Figure 1. Region of favorable visibility for near-Earth RSO observations above a minimum elevation angle of 20°.

3. Geometrical Model for RSO Coverage and Observatory Separation

The minimum elevation constraint described in the previous section can be translated into a geometrical model that relates RSO altitude and minimum elevation angle

to the coverage provided by each observatory and to the required separation between neighboring stations.

The present study focuses on RSOs located from very low altitudes up to 2000 km, a range that includes a large fraction of the space-debris population of interest for surveillance and tracking applications [38,39]. The observation and trajectory determination of these objects are strongly constrained by the capabilities of the ground-based observatories and telescopes used for their detection and tracking [14]. Their generally small size and large population also make wide-field optical systems particularly useful for detection and identification [40]. In addition, the motion of low-altitude debris can be significantly affected by perturbations such as atmospheric drag and solar radiation pressure, which complicate the prediction of their trajectories [39]. These characteristics reinforce the interest in geographically distributed observatory networks, which can provide complementary observations and improve the determination and monitoring of RSO trajectories, including objects undergoing atmospheric re-entry.

Assuming a spherical Earth with radius r_t = 6378 km, the geometrical visibility of an RSO at altitude h can be described as a function of the minimum elevation angle ϕ (Figure 2). The observation cone (with angle θ) is directly determined by an angle ϕ above the horizon, as shown in Figures 1 and 2. Furthermore, the angle α relative to the center of the Earth that the observation of the RSO covers can be defined. The following expressions involving these variables can be derived:

$$\frac{r_t + h}{\sin\left(\pi - \frac{\theta}{2}\right)} = \frac{r_t}{\sin\left(\frac{\theta}{2} - \frac{\alpha}{2}\right)}, \tag{1}$$

$$\alpha = \theta - 2\arcsin\left(\frac{r_t \sin\left(\frac{\theta}{2}\right)}{r_t + h}\right). \tag{2}$$

The angle α defines the angular extent of the visibility region of an observatory for a given altitude h and could be taken as a starting point for constructing a system that covers the entire surface of the Earth or large areas of it. It should also be noted that the surface of a sphere cannot be covered by circular observation areas without some overlapping between them.

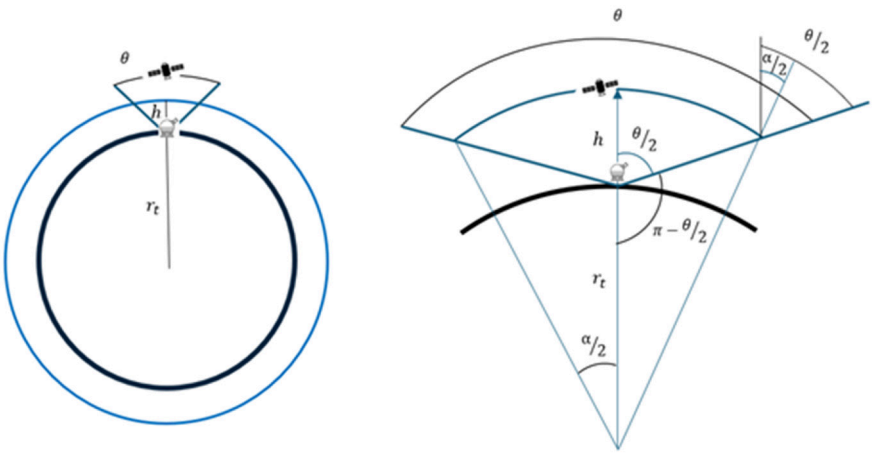


Figure 2. Sketch of the Earth and the observation cone of an RSO at altitude h (**left**). The geometrical relationships between the Earth radius r_t, the RSO altitude h, and the angles θ and α are shown in detail on the (**right**).

Figure 3 illustrates the proposed approach to maintaining visibility of an RSO, in which two or more ground-based observatories combine their observable regions of the sky. By overlapping their fields of view, it is possible to compensate for the lower region of poor visibility (minimum of 20°) by appropriately combining the regions of good visibility from both observatories [38]. With this distribution of observatories, it will be geometrically possible to track an object continuously while avoiding observations at unfavorable angles (Figure 1). The angle β, which relates to the distance to the boundary between the two observation areas, is shown in Figure 3 and depends on the other variables through the following expressions:

$$\tan\left(\frac{\alpha}{2}\right) = \frac{l}{d}\tan\left(\frac{\beta}{2}\right) = \frac{2}{\sqrt{3}}\tan\left(\frac{\beta}{2}\right), \tag{3}$$

$$\beta = 2\arctan\left(\frac{\sqrt{3}}{2}\tan\left(\frac{\alpha}{2}\right)\right), \tag{4}$$

$$\beta = 2\arctan\left(\frac{\sqrt{3}}{2}\tan\left(\frac{\theta}{2} - \arcsin\left(\frac{r_t \sin\left(\frac{\theta}{2}\right)}{r_t + h}\right)\right)\right). \tag{5}$$

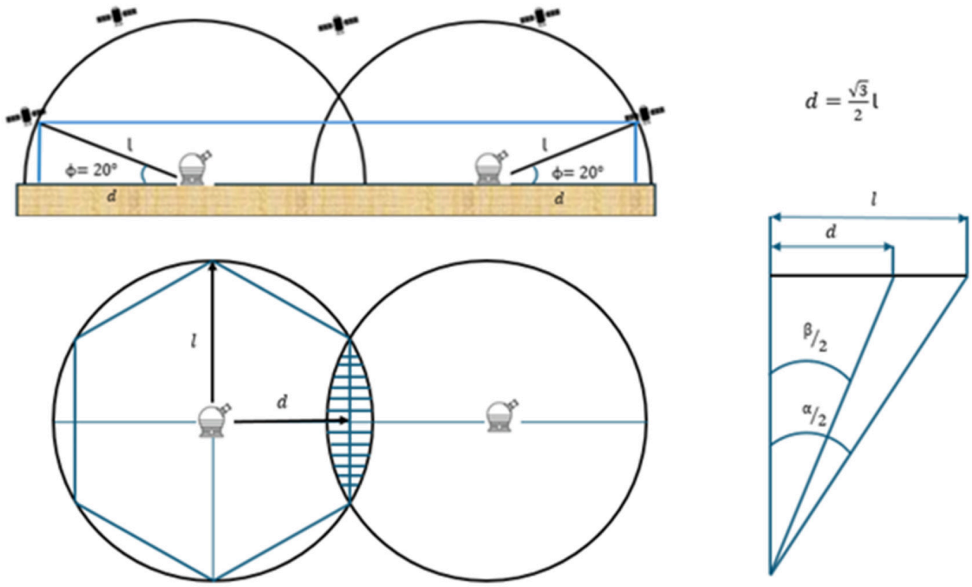


Figure 3. Arrangement of two observatories overlapping their lower field of view (20° above the horizon, see Figure 1) to achieve optimal sky visibility (**left**). The overlap zone (**left**), the relationship between the distances d and l (**right**), and the hexagon of the corresponding Goldberg polyhedron are indicated (**left**).

4. Geometrical Configurations for Global Observatory Networks

Figure 3 shows that, by appropriately positioning the observatories, large areas of the Earth's surface can be covered using an approximately hexagonal distribution. However, this type of regular arrangement cannot be extended directly to the entire Earth, since a spherical surface cannot be completely covered by regular hexagonal tiles of equal size. To overcome this geometrical limitation while maintaining the spacing requirements derived in the previous section, two alternative approaches are considered in this work: Goldberg polyhedra and Voronoi tessellations.

4.1. Goldberg Distribution

As a first approach to overcoming this difficulty, Goldberg polyhedra are considered. By taking the largest hexagonal cell and ensuring that it remains within the useful visibility region of the corresponding observatory, these polyhedra can be used to construct a global distribution of stations with nearly uniform spacing and to determine suitable observatory locations over the Earth's surface (Figure 4).

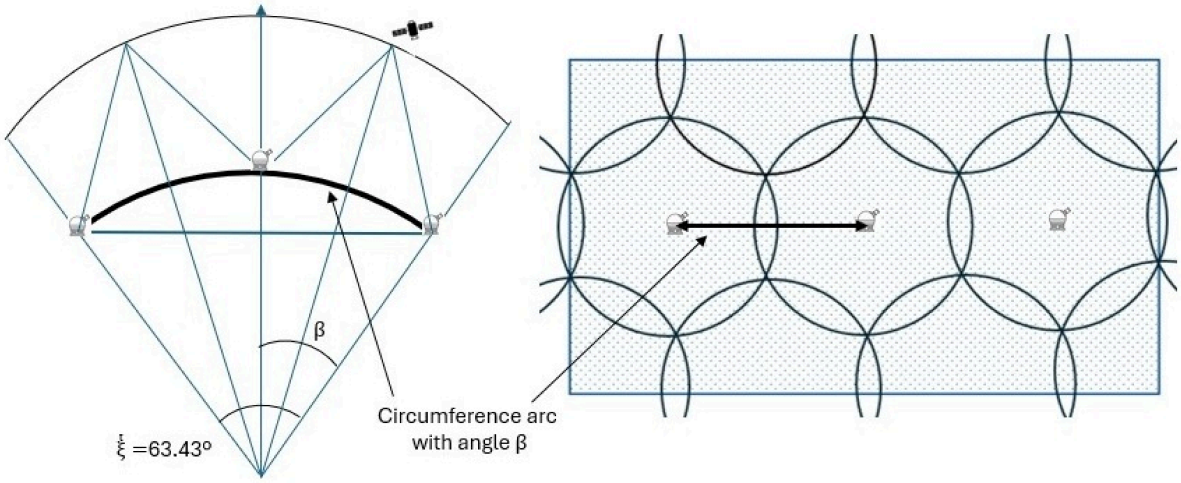


Figure 4. Geometrical separation between two observatories considering the arc of circumference between them (**left**), and corresponding distribution based on the Goldberg polyhedra with the same distance between them (**right**).

Figure 5 shows two examples of Goldberg polyhedra that cover a sphere. These polyhedra were proposed by Michael Goldberg in 1935 [31], and can be used to cover a sphere with regular and semi-regular hexagons and pentagons. In particular, class I polyhedra, that is, those of frequency (M, 0), are the most symmetrical, especially as the order of these polyhedra increases.

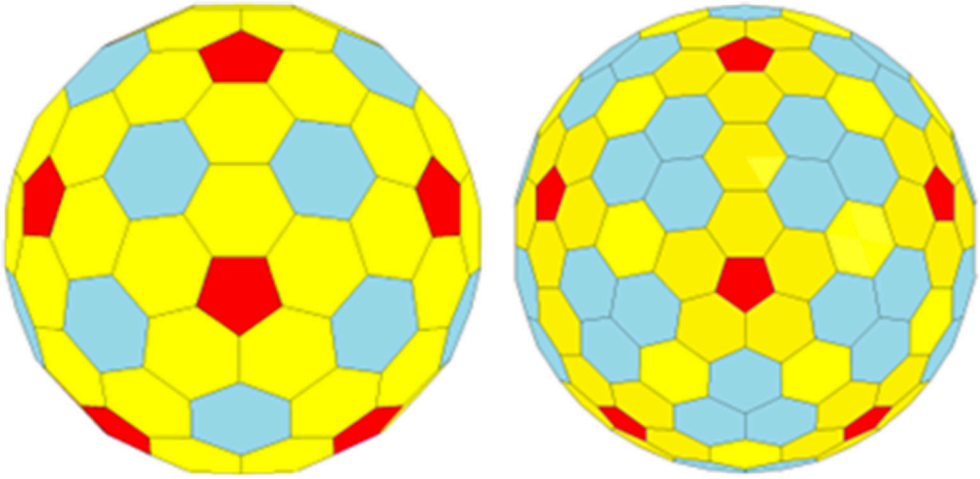


Figure 5. Examples of Goldberg polyhedra of order (3,0) and (4,0) ((**left**) and (**right**), respectively). Author: Tom Ruen. Source: Wikimedia Commons.

These polyhedra also have exactly 12 pentagons whose centers lie at the vertices of an icosahedron inscribed in the sphere. As can be seen in Figure 5, between each pair of adjacent pentagons there are exactly M–1 hexagons, where M is the order of the polyhedron (M, 0). Below, we propose a simple method for estimating the number of observatories

required, N_{obs}, as a function of the angle β, obtained in Section 3. This is equivalent to saying that N_{obs} can be expressed in terms of the minimum elevation of observation above the horizon, ϕ, and the altitude of the orbit to be observed, h.

For a class I Goldberg polyhedron of frequency (M, 0), the number of faces N_f is given by [28]:

$$N_f = 2 + 10\mathrm{M}^2, \tag{6}$$

The angular separation between two adjacent vertices of the underlying icosahedron is:

$$\xi = arccos\frac{1}{\sqrt{5}} = 1.1071 \text{ rad} = 63.43^\circ \tag{7}$$

and the approximate relation between this angular separation and the Goldberg order M is:

$$\mathrm{M} = \frac{\xi}{\beta}, \tag{8}$$

An approximate method for calculating the order M of the polyhedron that can be built with observatories characterized by the angle β follows from taking M as the smallest integer greater than the result of Equation (8). This is a spacing criterion: it makes the separation between neighboring stations close to β but, as shown in Section 6, it does not by itself guarantee that every point of the sphere is covered. From this order, it is easy to use Equation (6) to calculate the required number of observatories to be distributed across the Earth's surface, N_{obs}, which equals the number of faces of the polyhedron:

$$N_{obs} = 2 + 10\mathrm{M}^2. \tag{9}$$

With this approach, the calculation of the distance between two observatories, equal to $2d$ (see Figure 3), at the center of their corresponding hexagon in the Goldberg polyhedron, will depend on the reduction in visibility, that is, on the angle ϕ shown in Figures 1 and 3, and can be easily calculated by multiplying the Earth's radius, r_t, by the angle β (see Figure 4). In what follows, the number of observatories, N_{obs}, is written simply as N.

RSOs in LEO are found at altitudes ranging from 150 km to approximately 2000 km [38]. Many of these objects form very large constellations [12] and are of particular interest because of their high concentration in orbit and their similar altitudes [15]. If we consider two visibility reductions (one more favorable and one less so), $\phi = 20^\circ$ and $\phi = 30^\circ$, depending on the altitude h considered for Space Surveillance and Tracking (SST), a different number of observatories, N, is obtained from the Goldberg polyhedron distribution. Table 1 shows the results for altitudes h = 100, 250, 500, 1000 and 2000 km.

Table 1. Distribution of observatories for SST of RSOs based on Goldberg polyhedra. Number of observatories N and spacing between them $2d$ as a function of the altitude of the RSO, h, and the minimum elevation angle above the horizon, ϕ (see Figure 1).

h [km]	$\phi = 20^\circ$		$\phi = 30^\circ$	
	$2d$ [km]	N	$2d$ [km]	N
100	444.2	2562	288.9	6252
250	1018.3	492	685.6	1212
500	1812.7	162	1269.3	362
1000	3041.2	92	2229.9	162
2000	4760.1	42	3648.1	42

4.2. Voronoi Distribution

As an alternative to the Goldberg-based distribution, Voronoi tessellations provide greater flexibility in the number of regions into which the spherical surface can be divided. Unlike Goldberg polyhedra, for which the number of faces is restricted by the discrete order M of the polyhedron, a Voronoi tessellation can be generated from an arbitrary number of sites. This makes it possible to construct network configurations with a number of observatories more closely adapted to the spacing requirements derived from the RSO altitude and minimum elevation angle.

A Voronoi diagram is defined from a set of generating points, or sites, in such a way that every point within a given region is closer to its corresponding site than to any other site [32]. Figure 6 illustrates this principle for a random set of points in the plane.

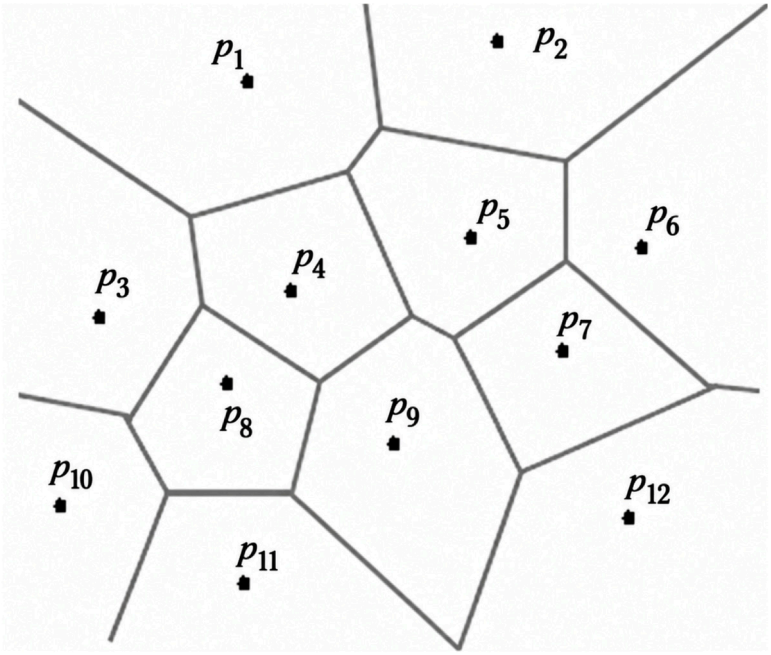


Figure 6. Voronoi diagram of a random set of points in the plane.

Let P = {p_1, p_2…p_n} be a set of *n* distinct points. The Voronoi diagram associated with P is defined as a subdivision of the domain into *n* cells, one for each point p_i, with the property that a point *q* belongs to the cell associated with p_i if and only if its distance to p_i is smaller than its distance to any other point in P [41].

In the present application, each generating point represents the location of an observatory, while the corresponding Voronoi cell represents the region associated with that station. For the Voronoi configuration, the N station locations are generated with a Fibonacci-sphere lattice, which provides a nearly uniform distribution of points for any N; the spherical Voronoi cells built around these points define the region assigned to each station and are used to display the resulting tessellation. The greater flexibility in the number of Voronoi cells makes it possible to adjust the network size more closely to the number of observatories required by the visibility constraints derived in Section 3.

In contrast to the Goldberg configuration, where increasing the network size requires moving from one discrete polyhedron order to the next, the Voronoi approach allows intermediate numbers of observatories to be considered. This provides a finer adjustment of the spatial distribution while maintaining nearly uniform separation between neighboring stations. Representative Voronoi distributions are shown in Figure 7.

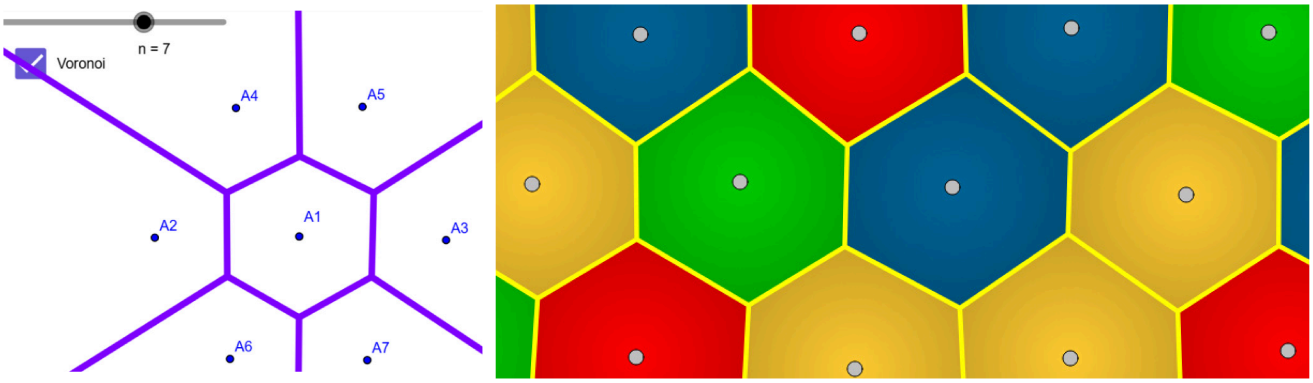


Figure 7. Examples of Voronoi diagrams for various locations. Source: https://www.geogebra.org.

The Voronoi-based approach therefore provides a more flexible alternative to the Goldberg distribution, allowing the number of observatory regions to be adjusted more closely to the network size required by the visibility constraints.

5. Geographical Optimization Procedure

Given the various options in Table 1, based on different configurations that depend on two minimum elevation angles and different RSO altitudes, together with the fact that water covers approximately 70% of the Earth's surface, an algorithm has been developed to incorporate these variables. The objective of the procedure is to identify, for each network configuration, the orientation that maximizes the number of observatory locations falling on land. The option to rotate each of the sites obtained relative to the Earth's center is incorporated, with the aim of maximizing the possibilities for siting the observatories on the Earth's surface.

For the Voronoi configuration, the required number of observatory locations is generated over the spherical surface using a Fibonacci-sphere distribution, as shown in (Figure 8a). For the Goldberg configuration, the optimal Goldberg frequency is first selected, followed by the generation of an icosahedral base, its geodesic subdivision, and the projection of the resulting vertices onto the spherical surface, as shown in (Figure 8b). In both cases, geometrical metrics are then computed for the resulting configurations: the ideal coverage angle ($\alpha/2$), the minimum angular separation between stations, the worst-case gap (the largest distance from a station to its nearest neighbor) and the covering radius (the largest distance from any point of the sphere to the nearest station).

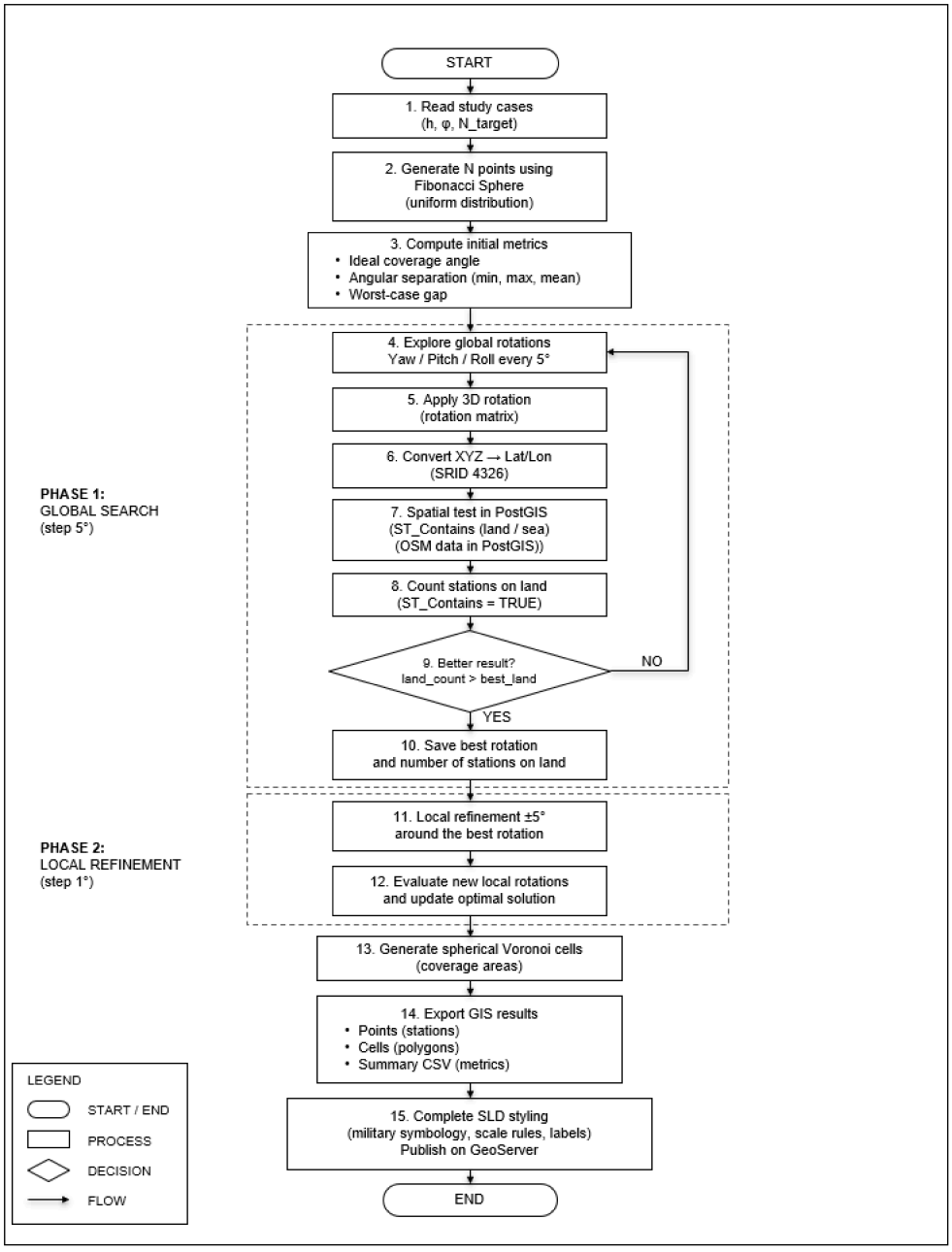
In order to process this large number of options and possibilities, the algorithm shown in Figure 8 performs the geographical evaluation using the Natural Earth land dataset (version 5.1.1, scale 1:10,000,000; https://www.naturalearthdata.com). Specifically, it uses the global landmass shapefile ne_10m_land.shp, which includes the main islands and many smaller ones, as the reference for determining whether each candidate observatory location falls on land or sea.

For each case considered in Table 1, defined by the RSO altitude and the minimum elevation angle, the complete set of observatory locations is iteratively rotated relative to the Earth's center. In the first stage, a global search is carried out using yaw, pitch and roll rotations with an angular step of 5° (93,312 orientations). For each orientation, the station coordinates are converted from Cartesian coordinates to latitude and longitude using SRID 4326. A spatial land/sea test based on ST_Contains is then applied in PostGIS, and the number of observatories located on land is counted. The orientation producing the largest number of land-based stations is retained as the best global solution.

A second stage performs a local refinement around this best global orientation. Rotations within $\pm 5°$ of the selected solution are evaluated using a finer angular step

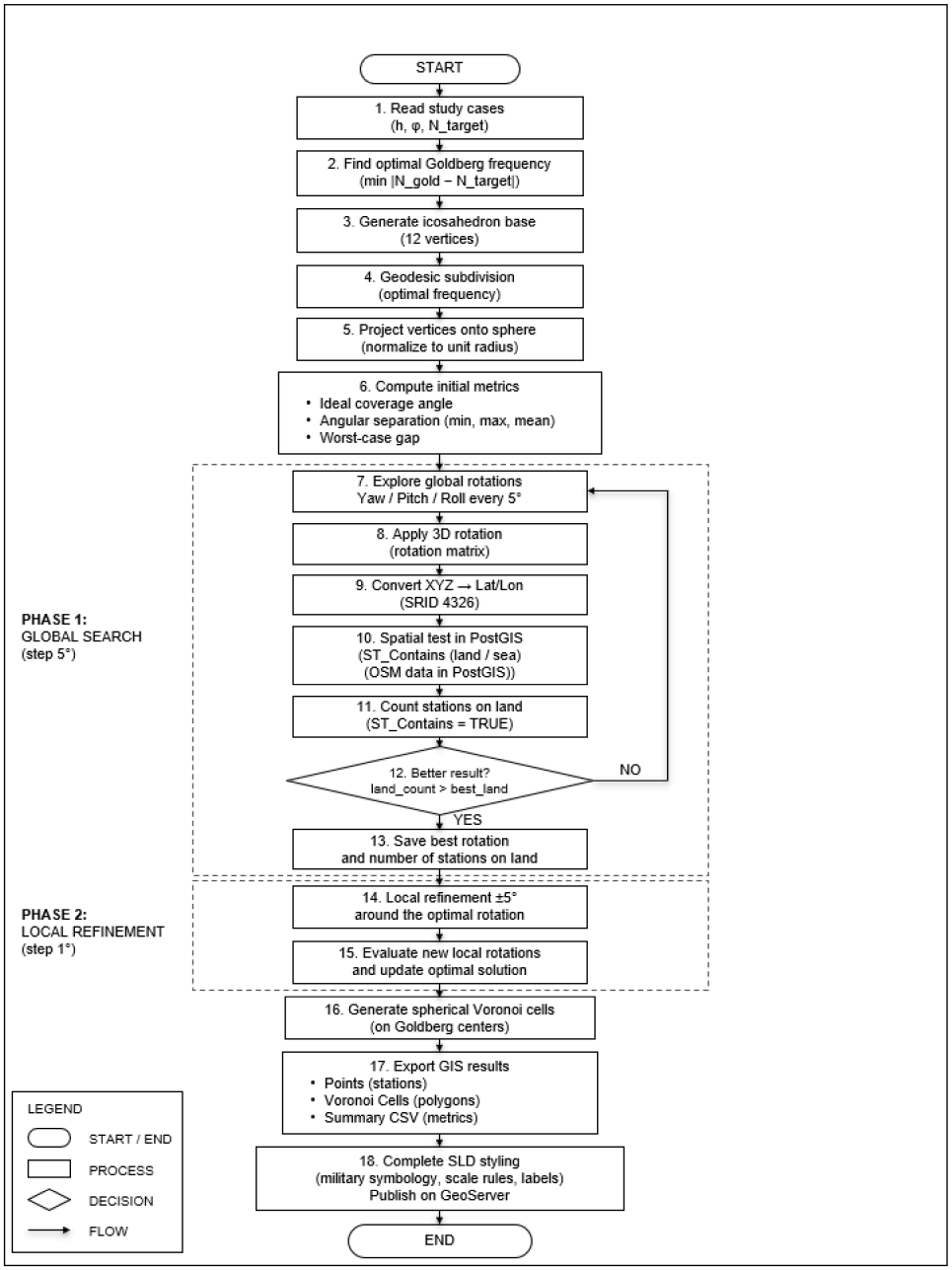
of 1° (11 × 11 × 11 = 1331 orientations). The new orientations are assessed using the same land/sea criterion, and the optimal configuration is updated whenever a greater number of observatories is located on land. The result is therefore the best orientation found by this search, not necessarily the global optimum.

Once the final orientation has been selected, spherical Voronoi cells are generated around the resulting observatory locations. The final station coordinates, cell geometries and summary metrics are then exported for GIS visualization and further analysis.



(**a**)

Figure 8. *Cont.*



(**b**)

Figure 8. Flow chart diagrams of the algorithm used by Voronoi and Goldberg ((**a**) Voronoi, (**b**) Goldberg Absolute) to determine the optimal distribution of ROSOs and to compare the two geometries.

6. Results

The main results obtained from applying the above algorithm are shown in Table 2, which gives, for each case in Table 1, the number and percentage of stations that fall on land for the best orientation found. The total number of land/sea tests carried out for each case is the number of stations N multiplied by the number of orientations evaluated (94,643). Since both configurations use the same number of stations N in each case, they are compared at equal network size, and the differences between them in Table 2 reflect how well each configuration fits the distribution of land for the best orientation found, not differences in network-size efficiency. The freedom of the Voronoi configuration to adopt intermediate values of N has not been exploited in Table 2, where N is set equal to that of the Goldberg configuration.

The spacing criterion of Equations (8) and (9) was checked on the resulting configurations with two metrics: the worst-case gap, defined as the largest distance between a station and its nearest neighbor, and the covering radius, defined as the largest distance from any point of the sphere to the nearest station. Both are independent of the orientation of the network. They are compared with the angular separation $\beta = 2d/r_t$ (Table 1) and with the visibility radius $\alpha/2$ (Section 3), respectively. The visibility radius $\alpha/2$ was computed with r_t = 6371 km in these calculations; using r_t = 6378 km (Section 3) changes $\alpha/2$ by about 0.1% and does not change any of the comparisons.

For the Voronoi configuration the worst-case gap does not exceed β in any of the ten cases, although for h = 100 km and $\phi = 20^\circ$ it is practically equal to it (3.97° against 3.99°). For the Goldberg configuration it exceeds β, by 5 to 18%, in the six cases with h $\leq$ 500 km. The covering radius exceeds $\alpha/2$ in seven of the ten Goldberg cases (by 9 to 19%: $h \leq 500$ km, and h = 2000 km with $\phi = 30^\circ$) and in nine of the ten Voronoi cases (by 4 to 34%); it is below $\alpha/2$ for the Goldberg configuration at h = 1000 km (both elevations) and at h = 2000 km with $\phi = 20^\circ$, and for the Voronoi configuration only at h = 2000 km with $\phi = 20^\circ$. For the most restrictive case (h = 100 km, $\phi = 30^\circ$, N = 6252), where $\beta = 2.60^\circ$ and $\alpha/2 = 1.50^\circ$, the worst-case gap is 3.02° (Goldberg) and 2.55° (Voronoi), and the covering radius is 1.75° and 1.98°, respectively. For the same number of stations, the covering radius of the Goldberg configuration is 11 to 16% smaller than that of the Voronoi configuration. Therefore, the numbers of stations in Table 1 are design estimates based on spacing, and they do not guarantee complete geometrical coverage in every case. Keeping the covering radius below $\alpha/2$ with Goldberg polyhedra requires 3612, 812 and 252 stations at h = 100, 250 and 500 km for $\phi = 20^\circ$, 9002, 1692 and 492 stations for $\phi = 30^\circ$, and 92 stations at h = 2000 km for $\phi = 30^\circ$.

Table 2. Results of the algorithm (Figure 8) for the best orientation found for each configuration. N is the number of stations (Table 1); "Stations on land" is the number of stations that fall on land for that orientation, and the percentage is this number divided by N. "Total tests" is $N \times$ 94,643 orientations (93,312 in the global search plus 1331 in the local refinement).

RSO Altitude (km)	ϕ (°)	N	Geometry Distribution	Stations on Land (%)	Stations on Land	Total Tests
100	30	6252	Goldberg	29.78	1862	591,708,036
			Voronoi	29.38	1837	591,708,036
	20	2562	Goldberg	30.29	776	242,475,366
			Voronoi	29.98	768	242,475,366
250	30	1212	Goldberg	31.02	376	114,707,316
			Voronoi	30.78	373	114,707,316
	20	492	Goldberg	32.72	161	46,564,356
			Voronoi	32.32	159	46,564,356
500	30	362	Goldberg	33.43	121	34,260,766
			Voronoi	33.15	120	34,260,766
	20	162	Goldberg	35.80	58	15,332,166
			Voronoi	36.42	59	15,332,166
1000	30	162	Goldberg	35.80	58	15,332,166
			Voronoi	36.42	59	15,332,166
	20	92	Goldberg	39.13	36	8,707,156
			Voronoi	41.30	38	8,707,156
2000	30	42	Goldberg	47.62	20	3,975,006
			Voronoi	50.00	21	3,975,006
	20	42	Goldberg	47.62	20	3,975,006
			Voronoi	50.00	21	3,975,006

The land optimization retains, for each configuration, the orientation that places the largest number of stations on land (between 29.4% and 50.0% of the stations, Table 2). The stations that fall at sea are not available, so the network formed only by land stations does not provide continuous global coverage: in the oceanic regions the distance between the remaining stations is larger than the design separation β. The numbers of stations in Table 1 therefore define the geometrical reference network, and Table 2 indicates the fraction of it that could be installed on land. Closing the oceanic gaps would require sites not considered in this study, such as islands, offshore platforms or ship-based stations.

Regional Case Studies

To better illustrate the practical application of this work, a comparative study is presented below between the Goldberg and Voronoi geometric distributions for three countries of different geographical sizes, chosen as examples of a large territory in the southern hemisphere (Australia), a medium-sized territory in the northern hemisphere (Ukraine) and a small territory in the equatorial region (Ecuador). The case analyzed is the most demanding one in Table 2: an altitude of 100 km and a minimum elevation of 30° (N = 6252).

In addition to the original global distributions, both algorithms (Voronoi and Goldberg) were run specifically for each country, using the same search procedure as in Section 5 (best of 94,643 orientations) and the same set of candidate orientations, but with the territory of each country, instead of the global land layer, as the reference for the land test. The national boundaries (administrative level 0) were taken from GADM version 4.1 (https://gadm.org), using the files gadm41_AUS_0, gadm41_ECU_0 and gadm41_UKR_0. The station distribution is not modified; the algorithm only adjusts the rotation of the global grid to the geography of each country, as shown in Table 3.

Table 3. Number of stations inside each country for the global runs and for the exclusive runs (algorithm run only for the territory of the country), for the Voronoi and Goldberg configurations (h = 100 km, $\phi = 30^\circ$, N = 6252).

Countries	Voronoi Global	Voronoi Exclusive	Goldberg Global	Goldberg Exclusive
Australia	98	103	102	121
Ukraine	8	12	5	14
Ecuador	2	6	3	7

In the three countries, running the algorithm exclusively for the territory increases the number of stations located inside it, as illustrated in Figure 9 for Australia: from 98 to 103 stations with the Voronoi configuration (+5.1%) and from 102 to 121 with the Goldberg configuration (+18.6%).

In Ukraine (Figure 10), the number of stations increases from 8 to 12 with the Voronoi configuration (+50%) and from 5 to 14 with the Goldberg configuration (+180%). In Ecuador (Figure 11), the number of stations increases from 2 to 6 with the Voronoi configuration (+200%) and from 3 to 7 with the Goldberg configuration (+133.3%).

These results show that, when the algorithm is applied to each territory individually, the number of stations inside it increases in the three cases. The relative increase is larger in Ukraine and Ecuador than in Australia, but it is computed on very small baselines (2 to 8 stations), so it has no statistical meaning, and the ranking is not monotonic with territory size (Table 3). The values are the best of 94,643 orientations for a single configuration (h = 100 km, $\phi = 30^\circ$), and they are illustrative only: they do not establish a general relationship between territory size and benefit, and they do not measure the coverage of each territory. The small number of stations that fit inside a small or medium-sized territory (between 2 and 14 stations in Ecuador and Ukraine) also illustrates that deploying such a network on land would require international collaboration.

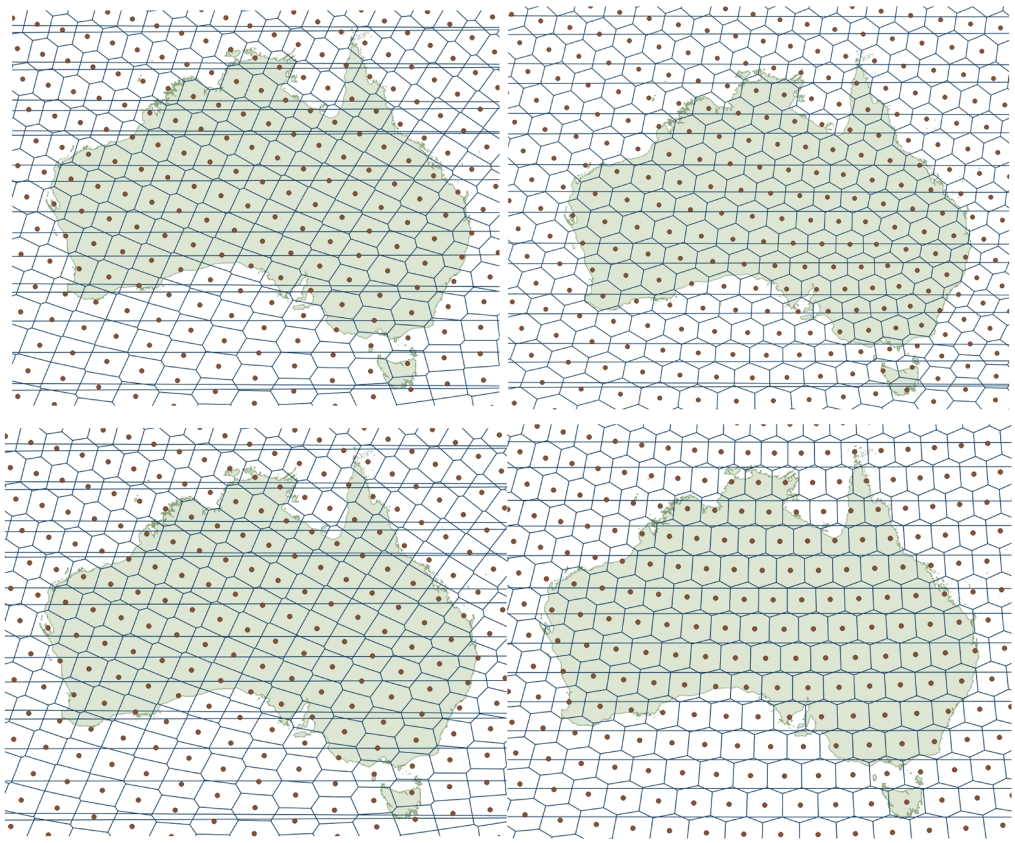


Figure 9. Distribution pattern in Australia, according to the global Goldberg map (**top left**) compared with the exclusive Goldberg map (**top right**) and the global Voronoi map (**bottom left**) and the exclusive Voronoi map (**bottom right**).

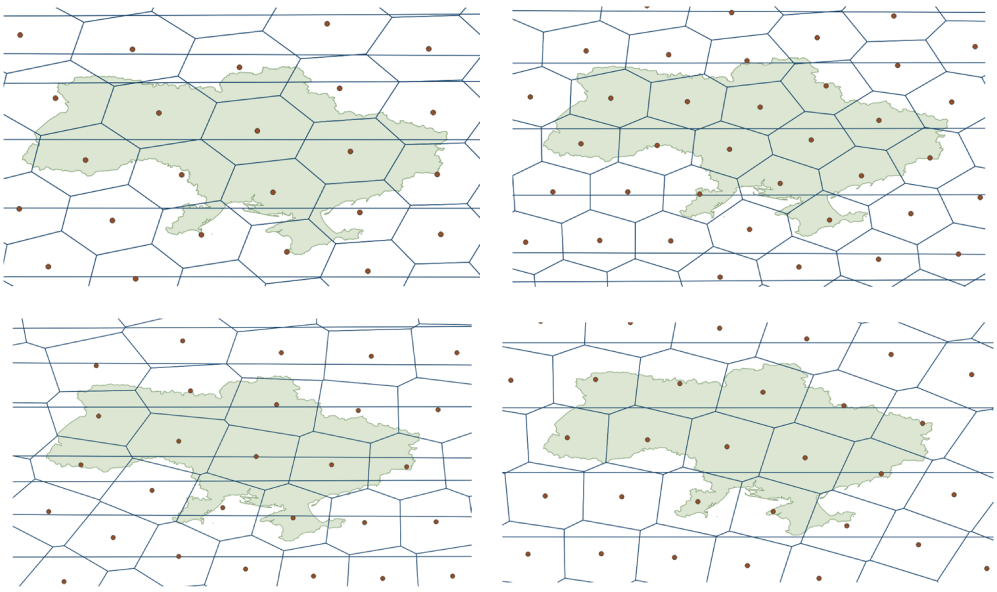


Figure 10. Distribution pattern in Ukraine, according to the global Goldberg map (**top left**) compared with the exclusive Goldberg map (**top right**) and the global Voronoi map (**bottom left**) and the exclusive Voronoi map (**bottom right**).

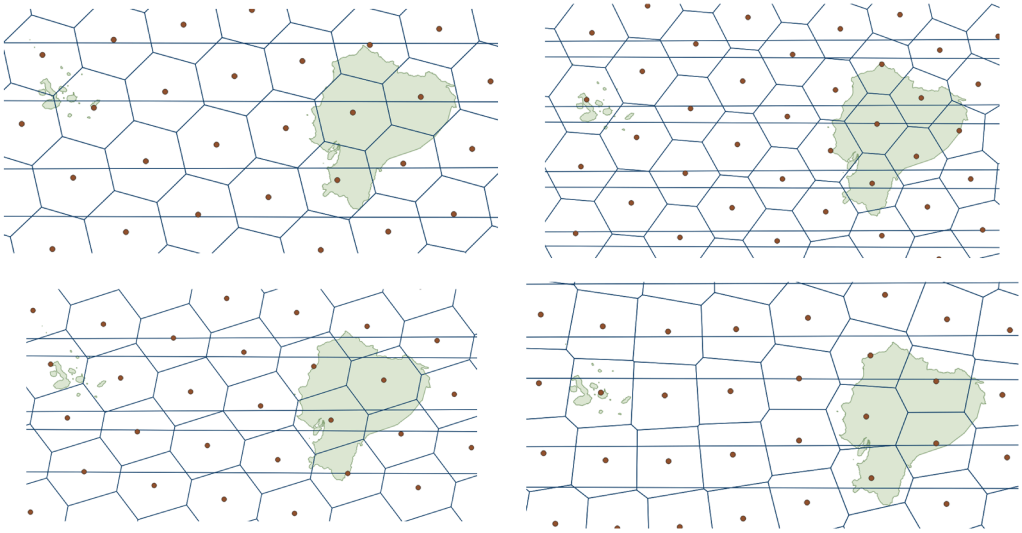


Figure 11. Distribution pattern in Ecuador, according to the global Goldberg map (**top left**) compared with the exclusive Goldberg map (**top right**) and the global Voronoi map (**bottom left**) and the exclusive Voronoi map (**bottom right**).

7. Conclusions

Robotic observatories offer an opportunity to build synchronized networks with large geographical coverage for the surveillance and tracking of RSOs. For such networks to provide geometrical coverage without gaps, however, the stations must be distributed efficiently over the Earth's surface while avoiding an unnecessary increase in their number. For such networks to provide geometrical coverage without gaps, however, the observatories must be distributed efficiently over the Earth's surface while avoiding an unnecessary increase in the number of stations. This work has addressed this problem through a geometrical framework based on visibility constraints, Goldberg polyhedra, and Voronoi tessellations.

The proposed methodology relates orbital altitude and minimum observation elevation to the angular separation required between observatories, enabling the estimation of both the number and geographical distribution of stations for the observation of RSOs, using a spacing criterion.

In the cases studied (h = 100–2000 km and $\phi = 20^\circ$ and 30°), the orbital altitude is the factor with the largest influence on the number of stations estimated with the spacing criterion, which decreases by a factor of 60 to 150 between 100 km and 2000 km. For objects at 100 km altitude, the number of observatories estimated ranges from 6252 stations for a minimum observation elevation of 30° to 2562 stations for 20°. As orbital altitude increases, the influence of atmospheric and visibility constraints decreases significantly, such that at 2000 km altitude both elevation criteria lead to the same estimate of only 42 stations. These 42 stations are the estimate given by the spacing criterion (see Table 1). For $\phi = 30^\circ$, keeping the covering radius below $\alpha/2$ with Goldberg polyhedra requires 92 stations at this altitude, whereas for $\phi = 20^\circ$ the 42 stations are sufficient.

From a geometrical perspective, each observatory covers a spherical cap above a minimum elevation, and neighboring stations must overlap to avoid gaps. This leads to nearly uniform spherical distributions based on hexagonal tilings (with 12 pentagons in the Goldberg case), whose centers correspond to the locations of the observatories. The spacing criterion used here does not, however, guarantee gap-free coverage in every case.

The projection of these geometrical configurations onto the Earth's surface made it possible to evaluate Goldberg and Voronoi tessellations as possible deployment frameworks. Both provide similar proportions of stations on land (between 29% and 50%, depending on the case), and the differences between them are small: Goldberg gives slightly higher

proportions up to 250 km (by 0.2 to 0.4 percentage points), the results are practically equivalent at 500 km (differences below 0.7 percentage points), and Voronoi gives slightly higher proportions from 1000 km (by 0.6 to 2.4 percentage points, corresponding to one or two stations). Given the small size of these differences, these results do not allow either configuration to be considered more efficient than the other.

The case studies developed for Australia, Ecuador, and Ukraine show that the proposed GIS-based search procedure can adapt the orientation of the geometrical networks to specific territories. For the case analyzed (h = 100 km, $\phi = 30°$), applying the algorithm exclusively to each country increased the number of stations located within its territory with respect to the global network, in the three countries and with both configurations: from 98 to 103 (Voronoi) and from 102 to 121 (Goldberg) in Australia, from 2 to 6 and from 3 to 7 in Ecuador, and from 8 to 12 and from 5 to 14 in Ukraine. The relative increase is larger in the smaller territories, where the global network has only a few stations; since only three countries and one configuration were analyzed, this should be taken as an illustration and not as a general relationship between territory size and benefit. In the three cases, the Goldberg configuration placed more stations inside each territory than the Voronoi one.

The design of the network is only the first step: once deployed, the measurements of the same RSO obtained by different stations must be associated and combined to determine its orbit. This is a classical problem of multi-sensor tracking and orbit determination, and the methods developed for the fusion of complementary sensor modalities in other fields [42] and for the operation control of autonomous robotic platforms [43] could also be adapted to the control and data processing of a fleet of robotic observatories. These aspects depend on the network geometry proposed here, but they are outside the scope of this work and are left for future studies.

The present study is restricted to geometrical visibility constraints. It does not incorporate the temporal and optical constraints that also determine whether an object can be observed, namely the night-time operation of the stations, the illumination of the object by the Sun and its passage through the Earth's shadow, and the sky brightness during twilight, nor operational factors such as cloud cover, meteorological conditions, atmospheric seeing, light pollution, terrain masking, infrastructure availability, or geopolitical considerations. In particular, if the stations are uniformly distributed over the sphere, at any instant only about 40% of them have the Sun more than 12° below the horizon (nautical twilight) and about 35% more than 18° below (astronomical twilight), independently of the season. For the network of 42 stations obtained at 2000 km, only about 15–17 stations would therefore be in darkness at a given time, and the number of stations able to observe a given RSO simultaneously is smaller still, because the object must also be illuminated. Therefore, the expressions "continuous observation" and "continuous tracking" refer here only to geometrical visibility, and the networks obtained should be regarded as a first-order geometrical design to be refined with these constraints. In addition, the stations located at sea are excluded from the land-based networks, which therefore do not provide continuous global coverage.

Overall, the proposed methodology provides a practical geometrical tool for the preliminary design of global and regional observatory networks and offers a quantitative basis for future SST infrastructures operating across a wide range of orbital altitudes.

Author Contributions: Conceptualization, F.E.; methodology, F.E., A.R.-J., J.C. and S.P.; validation, F.E., A.R.-J., J.C. and S.P.; investigation, F.E.; resources, F.E. and A.R.-J.; data curation, F.E.; writing—original draft preparation, F.E., J.C. and S.P.; writing—review and editing, F.E., J.C. and S.P.; visualization, F.E., J.C. and S.P.; supervision, J.C. and S.P. All authors have read and agreed to the published version of the manuscript.

Funding: This research received no external funding.

Data Availability Statement: The data supporting this study's findings are available from the authors upon reasonable request.

Acknowledgments: The authors are grateful to Ángel Sanz Andrés for supporting the research activities on space engineering carried out at the IDR/UPM Institute over the past two decades. The authors are also indebted to the reviewers for their help in improving this paper.

Conflicts of Interest: The authors declare no conflicts of interest.

References

1. Ceplecha, Z. Photographic Geminids 1955. *Bull. Astron. Inst. Czech.* **1957**, *8*, 51.
2. Borovička, J. *Astrometry with All-Sky Cameras*; Astronomical Institute of the Czechoslovak Academy of Sciences: Prague, Czech Republic, 1992; Volume 79.
3. Ceplecha, Z. Geometric, Dynamic, Orbital and Photometric Data on Meteoroids from Photographic Fireball Networks. *Bull. Astron. Inst. Czech.* **1987**, *38*, 222–234.
4. Borovička, J.; Spurný, P.; Keclíková, J. A New Positional Astrometric Method for All-Sky Cameras. *Astron. Astrophys. Suppl.* **1995**, *112*, 173–178.
5. Jenniskens, P. *Meteor Showers and Their Parent Comets*; Cambridge University Press: Cambridge, UK, 2006; ISBN 9781316347823.
6. Espartero, F.Á.; Martínez, G.; Frías, M.; Montes Moya, F.S.; Castro-Tirado, A.J. Autonomous Spectrographic System to Analyze the Main Elements of Fireballs and Meteors. *Earth Planets Space* **2018**, *70*, 1–7. [CrossRef]
7. Espartero Briceño, F.Á. Sistemas Astronómicos de Gran Campo y Su Aplicación al Estudio de Meteoroides En La Atmósfera Terrestre. Ph.D. Thesis, Universidad Complutense de Madrid, Madrid, Spain, 2018.
8. Clemens, S.D. On-Orbit Resident Space Object (RSO) Detection Using Commercial Grade Star Trackers. Ph.D. Thesis, York University, Toronto, ON, Canada, 2019.
9. Cook, A.F.; Millman, P.M. Photometric Analysis of a Spectrogram of a Perseid Meteor. *Astrophys. J.* **1955**, *121*, 250. [CrossRef]
10. Kabelac, J. Shadow Function-Contribution to the Theory of the Motion of Artificial Satellites. *Bull. Astron. Inst. Czech.* **1988**, *39*, 213–220.
11. Le Xuan, H.; Tien, S.N.; Hoang, Q.T.; Van, K.T.; Anh, T.T.; La Thuy, L. A Study on Observing, Detecting, and Determining Objects in Low Earth Orbit Using Optical Telescope System. *Bull. Electr. Eng. Inform.* **2024**, *13*, 4456–4465. [CrossRef]
12. Deng, R.; Di, B.; Zhang, H.; Kuang, L.; Song, L. Ultra-Dense LEO Satellite Constellations: How Many LEO Satellites Do We Need? *IEEE Trans. Wirel. Commun.* **2021**, *20*, 4843–4857. [CrossRef]
13. Yurasov, V.S.; Shargorodskiy, V.D. The Optical Survey Aspects of Space Debris in LEO. In Proceedings of the Eighth US/Russian Space Surveillance Workshop, Arlington, VA, USA, 19–21 April 2010.
14. Potter, A.E. Ground-Based Optical Observations of Orbital Debris: A Review. *Adv. Space Res.* **1995**, *16*, 35–45. [CrossRef]
15. Yanagisawa, T.; Kurosaki, H.; Oda, H.; Tagawa, M. Ground-Based Optical Observation System for LEO Objects. *Adv. Space Res.* **2015**, *56*, 414–420. [CrossRef]
16. Villarroel, B.; Mattsson, L.; Guergouri, H.; Solano, E.; Geier, S.; Dom, O.N.; Ward, M.J. A Glint in the Eye: Photographic Plate Archive Searches for Non-Terrestrial Artefacts. *Acta Astronaut.* **2022**, *194*, 106–113. [CrossRef]
17. Hasenohr, T. *Initial Detection and Tracking of Objects in Low Earth Orbit*; German Aerospace Center: Stuttgart, Germany, 2016.
18. Bassa, C.G.; Hainaut, O.R.; Galadí-Enríquez, D. Analytical Simulations of the Effect of Satellite Constellations on Optical and Near-Infrared Observations. *Astron. Astrophys.* **2022**, *657*, A69. [CrossRef]
19. Campbell-Brown, M.D. Optical Observations of Meteors. *Earth Moon Planets* **2004**, *95*, 521–531. [CrossRef]
20. Molotov, I.; Agapov, V.; Kouprianov, V.; Titenko, V.; Rumyantsev, V.; Biryukov, V.; Borisov, G.; Burtsev, Y.; Khutorovsky, Z.; Kornienko, G.; et al. ISON Worldwide Scientific Optical Network. In *Proceedings of the Fifth European Conference on Space Debris, Darmstadt, Germany, 30 March–2 April 2009*; ESA Special Publication: Paris, France, 2009; Volume 672.
21. Guo, X.; Gao, P.; Shen, M.; Yang, D.; Yu, H.; Liu, T.; Li, J.; Zhao, Y. Introduction to APOSOS Project: 15 Cm Aperture Electro-Optical Telescopes to Track Space Objects. *Adv. Space Res.* **2020**, *65*, 1990–2002. [CrossRef]
22. Urru, A.; Spanu, M.; Congiu, E.; Palmas, A.; Andronico, P. Performance Index of a Network of Ground-Based Optical Sensors for Space Objects Observation and Measurements. *Adv. Space Res.* **2023**, *72*, 4147–4156. [CrossRef]
23. Lei, X.; Lao, Z.; Liu, L.; Chen, J.; Wang, L.; Jiang, S.; Li, M. Telescopic Network of Zhulong for Orbit Determination and Prediction of Space Objects. *Remote Sens.* **2024**, *16*, 2282. [CrossRef]
24. Castro-Tirado, A.J.; Soldán, J.; Bernas, M.; Páta, P.; Rezek, T.; Hudec, R.; Sanguino, T.M.; De La Morena, B.; Berná, J.A.; Rodríguez, J.; et al. The Burst Observer and Optical Transient Exploring System (BOOTES). *Astron. Astrophys. Suppl. Ser.* **1999**, *138*, 583–585. [CrossRef]

25. Castro-Tirado, A.J. Robotic Astronomy and the BOOTES Network of Robotic Telescopes. *Acta Polytech.* **2011**, *51*, 16–20. [CrossRef] [PubMed]
26. Espartero, F.; Cubas, J.; Pindado, S. Determination and Progress in Establishing the Robotic Observatory of Space Objects (ROSO). *Machines* **2026**, *14*, 532. [CrossRef]
27. Vavilova, I.; Elyiv, A.; Dobrycheva, D.; Melnyk, O. The Voronoi Tessellation Method in Astronomy. In *Intelligent Astrophysics*; Springer International Publishing: Cham, Switzerland, 2021; pp. 57–79.
28. Budavári, T.; Szalay, A.S.; Fekete, G. Searchable sky coverage of astronomical observations: Footprints and exposures. *Publ. Astron. Soc. Pac.* **2010**, *122*, 1375–1388. [CrossRef]
29. Pałka, P.; Olszewski, R.; Wendland, A. Using Spatial Data Science in Energy-Related Modeling of Terraforming the Martian Atmosphere. *Energies* **2022**, *15*, 4957. [CrossRef]
30. Hart, G. Goldberg Polyhedra. In *Shaping Space: Exploring Polyhedra in Nature, Art, and the Geometrical Imagination*; Springer: Berlin/Heidelberg, Germany, 2012; pp. 125–138.
31. Goldberg, M. The Isoperimetric Problem for Polyhedra. *Tohoku Math. J. First Ser.* **1935**, *40*, 226–236.
32. Fortune, S. A Sweepline Algorithm for Voronoi Diagrams. In Proceedings of the Second Annual Symposium on Computational Geometry, Philadelphia, PA, USA, 2–4 June 1986; pp. 313–322.
33. Espartero, F.; Cubas, J.; Nespral, D.; Pindado, S. New Astronomical Observatory Design for the Detection and Tracking of Satellite Objects: The Satellite Robotic Observatory (SRO). *Remote Sens.* **2024**, *16*, 4206. [CrossRef]
34. Corbard, T.; Ikhlef, R.; Morand, F.; Meftah, M.; Renaud, C. On the Importance of Astronomical Refraction for Modern Solar Astrometric Measurements. *Mon. Not. R. Astron. Soc.* **2019**, *483*, 3865–3877. [CrossRef]
35. Schildknecht, T. Optical Surveys for Space Debris. *Astron. Astrophys. Rev.* **2007**, *14*, 41–111. [CrossRef]
36. Tommei, G.; Milani, A.; Rossi, A. Orbit Determination of Space Debris: Admissible Regions. *Celest. Mech. Dyn. Astron.* **2007**, *97*, 289–304. [CrossRef]
37. Hamidian, S.; Kosari, A.R.; Assadian, N. An Optical Space-Based Surveillance Network for Tracking LEO Debris. *IEEE Aerosp. Electron. Syst. Mag.* **2024**, *39*, 18–35. [CrossRef]
38. Sampaio, J.C.; Wnuk, E.; De Moraes, R.V.; Fernandes, S.S. Resonant Orbital Dynamics in LEO Region: Space Debris in Focus. *Math. Probl. Eng.* **2014**, *929810*. [CrossRef]
39. Baker-McEvilly, B.; Bhadauria, S.; Canales, D.; Frueh, C. A Comprehensive Review on Cislunar Expansion and Space Domain Awareness. *Prog. Aerosp. Sci.* **2024**, *147*, 101019. [CrossRef]
40. Sun, R.; Yu, S.; Zhao, C.; Zhang, W. Algorithms for Surveying and Cataloguing Space Debris Utilizing a Wide Field of View Telescope. *Publ. Astron. Soc. Jpn.* **2019**, *71*, 67. [CrossRef]
41. Berg, M.; van Kreveld, M.; Overmars, M.; Schwarzkopf, O. *Computational Geometry: Algorithms and Applications*; Springer: Berlin/Heidelberg, Germany, 2000; p. 148.
42. Liu, X.; Li, Z.; Zhou, Y.; Peng, Y.; Luo, J. Camera–radar fusion with modality interaction and radar Gaussian expansion for 3D object detection. *Cyborg Bionic Syst.* **2024**, *5*, 0079. [CrossRef] [PubMed]
43. Sun, L.; Wang, Y.; Hui, X.; Ma, X.; Bai, X.; Tan, M. Underwater robots and key technologies for operation control. *Cyborg Bionic Syst.* **2024**, *5*, 0089. [CrossRef] [PubMed]

Disclaimer/Publisher's Note: The statements, opinions and data contained in all publications are solely those of the individual author(s) and contributor(s) and not of MDPI and/or the editor(s). MDPI and/or the editor(s) disclaim responsibility for any injury to people or property resulting from any ideas, methods, instructions or products referred to in the content.